B. Gantry rotation speed measurement (rotational stability)

Figure 7 shows the gantry position (degree) and the time from the gantry rotation start position. The solid lines in the figure express the theoretical values on the basis of the assumption that the gantry rotational speed is constant. There is good agreement between the measured and theoretical values for rotational speeds of 15 to 60 sec/revolution, and these are constant for all rotational speeds. Thus, regarding the appropriate gantry angles for rotating back the images, it turned out that the nominal gantry rotation angles are useful.

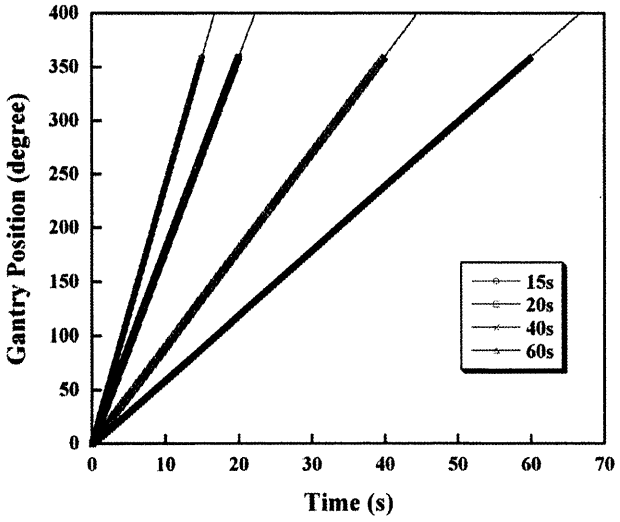

FIG. 7. Stability of the gantry rotational speed. The solid axis represents the theoretical value.

C. Binary MLC QA using the cylindrical scintillator

Figure 8 shows the ROC curves for the simple model and the clinical model. Setting the threshold, Th, too high, would give a false value. Setting the threshold too low results in spurious signals being detected on each ROI. This is also affected by the leaf open time. It is important, therefore, for us to consider the optimum Th value to make an adequate balance between sensitivity and specificity. Therefore, we employed the Youden index,[34] which is calculated from "sensitivity+specificity-1" and ranges from 0 to 1. We believe that the maximum Youden index represents the optimum Th in this case. From the results of the simple model, the maximum value is 0.987 when Th is at the 44 pixel value, with the sensitivity being 0.998 and the specificity 0.989. According to Fig. 5, Th = 44 pixel value is for the case for which between 2 and 4 leaves are open. However, in the case of one leaf only open, the detected light per frame is 29.1 pixel value (Fig. 5). Thus, if the value of Th = 44 pixel value were to be used, the case of one leaf open might be identified as not open.

In the clinical case, the maximum Youden index is 0.992 at Th = 28 pixel value. As shown in Fig. 5, Th = 28 pixel value is less than the measured value with one leaf open (29.1 pixel value). In the clinical model, the beam intensity generated from each binary MLC is modulated, even though leaves neighboring each other are open; it is not uncommon for each leaf open time to be different. Looking at the leaf open times frame by frame (every 33 msec), we can see when only one leaf is open. Therefore, we consider that Th = 28 pixel value, with which we are able to detect even one leaf open, is the most appropriate value. From the observations, the appropriate Th itself actually varies depending on the variation in the leaf pattern. Nevertheless, we believe that Th = 28 pixel value is the appropriate value because with it, the one leaf open status can be detected and its flexibility makes it applicable for any leaf pattern.

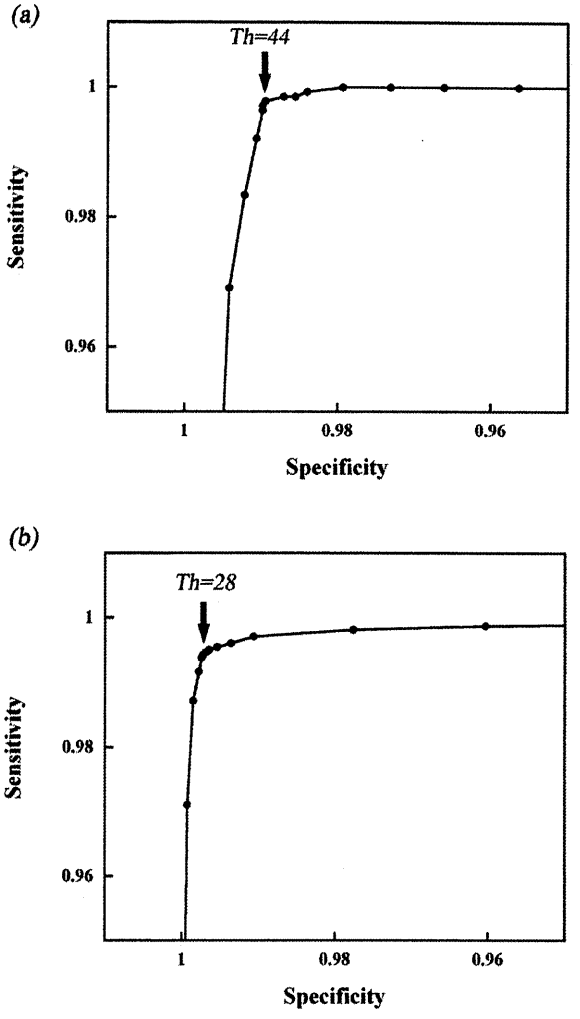

FIG. 8. ROC curves for a simple binary MLC pattern model (a) and a clinical binary MLC pattern model (b). The Youden index is at its maximum value at Th = 44 pixel value in the simple model and at Th = 28 pixel value in the clinical model.

Figure 9(a) shows the leaf open patterns expressed as original sinogram. Figure 9(b) is the reconstructed sinogram from measured projection datasets. The sensitivity and specificity are 1.000 and 0.919, respectively. Figure 9(c) shows the relative error. The relative error was calculated from the difference between Fig. 9(a) and Fig. 9(b), and was divided by the maximum value for each projection. Figure 9(d) represents a histogram of the values in Fig. 9(c). The error associated with the leaf open time is calculated from the mean and standard deviation of the relative errors. The calculation result was -1.3 ± 7.5%, and this is defined as the leaf open error. The 68.6% of all observed leaves were performed within ± 3% relative error. In some ROIs, the light measured was above the threshold but the leaf at the corresponding position was not open. This was due to field edge light from other leaf positions pushing the value of Q_j over the threshold value. This was very obvious in the case of ROI_j with the leaf numbers j+1 and j-1 open and j closed.

The sinogram clinically used for a prostate cancer patient is shown in Fig. 10(a); Fig. 10(b) is the reconstructed data from the measurement. The sensitivity and specificity are 0.994 and 0.997, respectively. The leaf open error was -3.4 ± 8.0%. The 77.5% of observed leaves were performed within ± 3% relative error. With respect to the errors, the status that some leaves

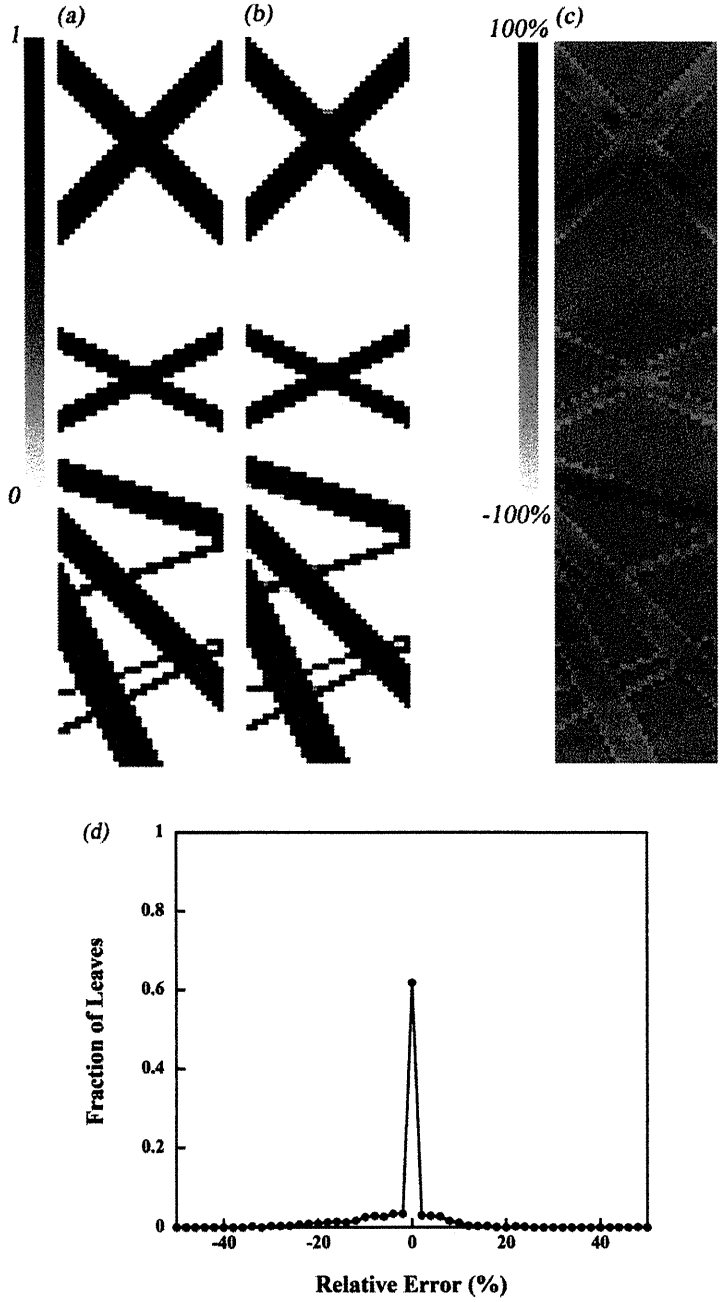

FIG. 9. Sinogram for planned simple binary MLC pattern model (a), measured sinogram (b), difference between these sinograms (c), and the resulting histogram (normalized) (d).

were open but not recognized as open occurred at a given leaf position because Q was below the threshold value. Conversely, the case in which leaves were not open but were recognized as open occurred around the same area of the simple sinogram result.

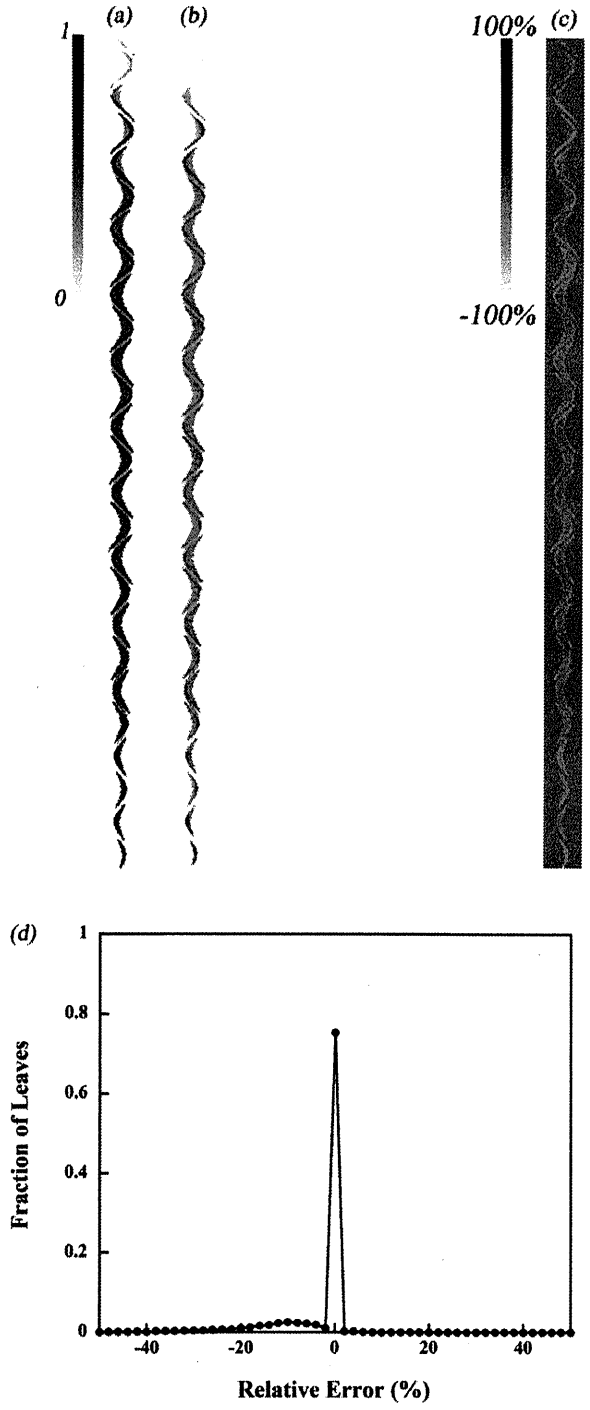

FIG. 10. Sinogram on planned clinical binary MLC pattern model (a), measured sinogram (b), difference between these sinograms (c), and the resulting histogram (normalized) (d).

IV. DISCUSSION

The leaf open errors were -1.3 ± 7.5% for the simple model and -3.4 ± 8.0% for the clinical model. The sensitivity and specificity were > 0.9, which means that the leaf status was correctly recognized in 90% of the cases. Hence the main reason for the detection errors might be caused by use of the formula used to convert detected light to leaf open time, which is based on the results of the 2.5 cm × 10 cm field measurement rather than the value of Th. As already shown in Fig. 5, the detected light changes depending on the field size, even though the leaf open time is constant. In the case of just one leaf being open, the detected light was 0.48 compared to the 10 cm field size. This change becomes more obvious for smaller field sizes. In the clinical model, the field size per frame is generally smaller than the simple field due to the intensity modulated field. This is why the error for the clinical model turned out to be -3.4 ± 8.0%, which is much larger than that for the simple model. Regarding the measured light correction, the light measurements obtained from sets of field sizes were normalized based on the light measured for the 10 cm field. However, for the leaf pattern for the simple model, scintillation light emitted from a corresponding leaf location was scattered in the medium and affected the adjacent leaf positions. The error associated with scattering varies depending on the field size and the scatter. Thus, ideally it would be preferable to calculate a variety of correction factors for any leaf pattern; this, however, is much too complicated.

We used the Youden index as a criterion in order to optimize the value of Th. The Youden index is computed from a comparison between the original sinogram and the sinogram delivered from the measurement. The Th value was originally supposed to be derived from a comparison between the original leaf pattern and the one from the measurement, by which the errors are also estimated. Nevertheless, since reliable measured data could not be obtained, we chose to use the planned sinogram as a reference value.

The errors in this study were caused by not using correction factors for Th depending on field size. If scattered light did not enter neighboring ROIs, no corrections associated with field size would be necessary. In such a situation, we could achieve accurate measurements and the errors would perhaps be independent of the Th value. In order to reduce the scattering, it might be a better solution to collimate the scattered light. Ikegami et al.[35] reported that it is possible to collimate the scintillation light and measure 3D dose distributions using scintillation fibers. If we were able to use scintillation fibers, it could be possible to perform our measurement with a higher accuracy.

Nevertheless, we have demonstrated that a simple measuring device using a combination of a camcorder and a cylindrical scintillator can work as a binary collimator QA device without light correction. With this device, measurements can be performed even in a clinical case with a sensitivity and specificity of more than 0.99 and a leaf open error of -3.4 ± 8.0%. Since the sensitivity and specificity are more than 0.99, and this measurement can identify the leaf positions where errors are most likely occur, we believe that this measurement can be used to detect leaf motion where the leaf is open but recognized as not so, or the opposite case.

In this study, we have used 20 cm diameter scintillator. It detected the radiation field only from leaf number 18 to leaf number 47. The binary MLC is composed of 64 leaves, which effectively makes a 40 cm field (in width) at isocenter. It would be preferable to use at least 40 cm diameter scintillator for all measurements. However, if such a detector were to be used for QA, it would be necessary to evaluate if our method would be applicable with a large scintillator size.

Kapatoes et al.[36] has reported a similar study where the sinogram is reconstructed using MIMiC MLC (Nomos Corporation, Pittsburgh, PA) and a CT detector, where the possibility of beam delivery similar to helical tomotherapy was investigated. Indeed it could be possible to do a similar trial with a helical tomotherapy unit. However, since the accelerator and CT detector are combined with an actuator and these are not independent, it is impossible to conduct the gantry angle check with this unit. Besides, it is difficult for users to make a use of the signal

obtained from a CT detector, which leads to a measurement lacking in versatility. The benefits of our method are that our unit can dynamically measure the motion of the binary leaves at any gantry angle (as well as the gantry position during rotation), and it provides simplicity of measurement. In this study, we accomplished observations of a binary MLC and the gantry angle easily with a simple unit consisting of a cylindrical scintillator and a general-purpose camcorder. We believe that this presents us with a very feasible QA tool.

V. CONCLUSIONS

We have developed a simple QA tool that can easily check binary MLC motion. This is composed of a cylindrical scintillator and a widely-used camcorder. The camcorder can monitor the binary MLC motion via scintillation light. Using the QA tool, we verified a simple binary MLC pattern and a more complicated MLC pattern used in clinic. In the sinogram of the simple binary MLC pattern, the leaves that were supposed to be open were detected with "open" status with respect to the detected light, and the sensitivity was 1.000. On the other hand, the leaves that were not supposed to be open were usually detected as such giving rise to a specificity of 0.919. The measurement was achievable with -1.3 ± 7.5% leaf open error. The 68.6% of observed leaves were performed within ± 3% relative error. In the clinical binary MLC pattern, the sensitivity and specificity were 0.994 and 0.997, respectively. The measurement could be performed with -3.4 ± 8.0% leaf open error. The 77.5% of observed leaves were performed within ± 3% relative error. These errors accounted for the values that are dependent on the planned leaf pattern. In order to remove such dependency, one needs to correct for the contribution of light scatter, which requires further study. The results of this study demonstrated that it is possible to dynamically detect the motion of a binary MLC, which is a difficult task with conventional film or ion chamber measurement. Our method has been investigated without couch motion, and we conclude that we are able to perform accurate verification with this constraint. Although this method is not a perfect alternative for QA, it is more easily performed than that which uses a combination of ion chamber and film measurements.

REFERENCES

1. Brahme A. Optimization of stationary and moving beam radiation therapy techniques. Radiother Oncol. 1988;12(2):129–40.
2. Bortfeld T, Burkelbach J, Boeseche R, Schlegel W. Method of image reconstruction from projections applied to conformation radiotherapy. Phys Med Biol. 1990;35(10):1423–34.
3. Webb S. Optimization by simulated annealing of three-dimensional conformal treatment planning for radiation fields defined by a multileaf collimator. Phys Med Biol. 1991;36(9):1201–26.
4. Webb S. Optimization by simulated annealing of three-dimensional, conformal treatment planning for radiation fields by a multileaf collimator: II. Inclusion of two-dimensional modulation of the x-ray intensity. Phys Med Biol. 1992;37(8):1689–704.
5. Balog J, Soisson E. Helical tomotherapy quality assurance. Int J Radiot Oncol Biol Phys. 2008;71(1 Suppl):S-13-S117.
6. Convery DJ, Rosenbloom ME. The generation of intensity-modulated fields for conformal radiotherapy by dynamic collimation. Phys Med Biol. 1992;37(6):1359–74.
7. Svensson R, Källman P, Brahme A. An analytical solution for the dynamic control of multileaf collimators. Phys Med Biol. 1994;39(1):37–61.
8. Stein J, Bortfeld T, Dörchel B, Schlegel W. Dynamic X-ray compensation for conformal radiotherapy by means of multi-leaf collimation. Radiother Oncol. 1994;32(2):163–73.
9. Spirou SV, Chui CS. Generation of arbitrary intensity profiles by dynamic jaws or multileaf collimators. Med Phys. 1994;21(7):1031–41.
10. Mackie TR, Holmes TW, Swerdloff S, et al. Tomotherapy: a new concept for the delivery of dynamic conformal radiotherapy. Med Phys. 1993;20(6):1709–19.
11. Mackie TR, Holmes TW, Reckwerdt PJ, Yang J. Tomotherapy: optimized planning and delivery of radiation therapy. Int J Imag Syst Technol. 1995;6(1):43–55.
12. Mackie TR, Balog J, Ruchala K, et al. Tomotherapy. Semin Radiat Oncol. 1999;9(1):108–17.

13. Herzen J, Todorovic M, Cremers F, et al. Dosimetric evaluation of a 2D pixel ionization chamber for implementation in clinical routine. Phys Med Biol. 2007;52(4):1197–208.
14. Bedford JL, Lee YK, Wai P, South CP, Warrington AP. Evaluation of the Delta4 phantom for IMRT and VMAT verification. Phys Med Biol. 2009;54(9):N167–N176.
15. Létourneau D, Publicover J, Kozelka J, Moseley DJ, Jaffray DA. Novel dosimetric phantom for quality assurance of volumetric modulated arc therapy. Med Phys. 2009;36(5):1813–21.
16. Yan G, Lu B, Kozelka J, Liu C, Li JG. Calibration of a novel four-dimensional diode array. Med Phys. 2010;37(1):108–15.
17. Knoll GF. Radiation detection and measurement, 3rd ed. New York (NY): John Wiley & Sons; 1999.
18. Beddar AS, Mackie TR, Attix FH. Water-equivalent plastic scintillation detectors for high-energy beam dosimetry: I. Physical characteristics and theoretical considerations. Phys Med Biol. 1992;37(10):1883–900.
19. Beddar AS, Mackie TR, Attix FH. Water-equivalent plastic scintillation detectors for high-energy beam dosimetry: II. Properties and measurements. Phys Med Biol. 1992;37(10):1901–913.
20. Lacroix F, Archambault L, Gingras L, Guillot M, Beddar AS, Beaulieu L. Clinical prototype of a plastic water-equivalent scintillating fiber dosimeter array for QA applications. Med Phys. 2008;35(8):3682–90.
21. Archambault L, Beddar AS, Gingras L, Lacroix F, Roy R, Beaulieu L. Water-equivalent dosimeter array for small-field external beam radiotherapy. Med Phys. 2007;34(5):1583–92.
22. Fukumura A, Noda Y, Omata K, et al. Simple range measurement of therapeutic ion beams using visible rays generated in a bare plastic scintillator block. Nucl Instrum Methods A. 1998;416(1):148–51.
23. Fukushima Y, Hamada T, Nishio T, Maruyama K. Development of an easy-to-handle range measurement tool using a plastic scintillator for proton beam therapy. Phys Med Biol. 2006;51(22):5927–36.
24. Kojima H, Hanada T, Katsuta S, Yorozu A, Maruyama K. New method for obtaining position and time structure of source in HDR remote afterloading brachytherapy unit utilizing light emission from scintillator. J Appl Clin Med Phys. 2009;10(3):86–95.
25. Petric MP, Robar JL, Clark BG. Development and characterization of a tissue equivalent plastic scintillator based dosimetry system. Med Phys. 2006;33(1):96–105.
26. Frelin AM, Fontbonne JM, Ban G, et al. The DosiMap, a new 2D scintillating dosimeter for IMRT quality assurance: characterization of two Cerenkov discrimination methods. Med Phys. 2008;35(5):1651–62.
27. Collomb-Patton V, Boher P, Leroux T, Fontbonne JM, Vela A, Batalla A. The DOSIMAP, a high spatial resolution tissue equivalent 2D dosimeter for LINAC QA and IMRT verification. Med Phys. 2009;36(2):317–28.
28. Beddar S, Archambault L, Sahoo N, et al. Exploration of the potential of liquid scintillators for real-time 3D dosimetry of intensity modulated proton beams. Med Phys. 2009;36(5):1736–43.
29. Boon SN, van Luijk P, Schippers JM, et al. Fast 2D phantom dosimetry for scanning proton beams. Med Phys. 1998;25(4):464–75.
30. Kodama K, Hamada M, Suzuki T, et al. Performance evaluation of X-ray CT using visible scintillation light [in Japanese]. Jpn J Radiol Technol. 2004;60(10):1429–36.
31. Archambault L, Briere TM, Beddar S. Transient noise characterization and filtration in CCD cameras exposed to stray radiation from a medical linear accelerator. Med Phys. 2008;35(10):4342–51.
32. Frelin AM, Fontbonne JM, Ban G, et al. Spectral discrimination of Cerenkov radiation in scintillating dosimeters. Med Phys. 2005;32(9):3000–06.
33. Archambault L, Beddar AS, Gingras L, Roy R, Beaulieu L. Measurement accuracy and Cerenkov removal for high performance, high spatial resolution scintillation dosimetry. Med Phys. 2006;33(1):128–35.
34. Youden WJ. Index for rating diagnostic trests. Cancer. 1950;3(1):32–35.
35. Ikegami K, Nishizawa H. Medical measurement of three dimensional depth dose profile using the plastic scintillation fiber block [in Japanese]. OYO BUTURI. 1998;67(6):682–86.
36. Kapatoes JM, Olivera GH, Ruchala KJ, Smilowitz JB, Reckwerdt PJ, Mackie TR. A feasible method for clinical delivery verification and dose reconstruction in tomotherapy. Med Phys. 2001;28(4):528–42.

Acta Oncologica, 2011; Early Online, 1–5

informa
healthcare

ORIGINAL ARTICLE

The relationship between the bladder volume and optimal treatment planning in definitive radiotherapy for localized prostate cancer

NAOKI NAKAMURA[1], NAOTO SHIKAMA[2], OSAMU TAKAHASHI[3], KENJI SEKIGUCHI[1], YUKIHIRO HAMA[4], KEIKO AKAHANE[1] & KEIICHI NAKAGAWA[5]

[1]*Department of Radiation Oncology, St. Luke's International Hospital, Tokyo, Japan,* [2]*Department of Radiation Oncology, Saitama Medical University, Hidaka, Japan,* [3]*Division of General Internal Medicine, Department of Medicine, St. Luke's International Hospital, Tokyo, Japan,* [4]*Department of Radiology, Edogawa Hospital, Tokyo, Japan and* [5]*Department of Radiology, Tokyo University School of Medicine, Tokyo, Japan*

Abstract

Background. There is no current consensus regarding the optimal bladder volumes in definitive radiotherapy for localized prostate cancer. The aim of this study was to clarify the relationship between the bladder volume and optimal treatment planning in radiotherapy for localized prostate cancer. *Material and methods.* Two hundred and forty-three patients underwent definitive radiotherapy with helical tomotherapy for intermediate- and high-risk localized prostate cancer. The prescribed dose defined as 95% of the planning target volume (PTV) receiving ≧ 100% of the prescription dose was 76 Gy in 38 fractions. The clinical target volume (CTV) was defined as the prostate with a 5-mm margin and 2 cm of the proximal seminal vesicle. The PTV was defined as the CTV with a 5-mm margin. Treatment plans were optimized to satisfy the dose constraints defined by in-house protocols for PTV and organs at risk (rectum wall, bladder wall, sigmoid colon and small intestine). If all dose constraints were satisfied, the plan was defined as an optimal plan (OP). *Results.* An OP was achieved with 203 patients (84%). Mean bladder volume (± 1 SD) was 266 ml (± 130 ml) among those with an OP and 214 ml (±130 ml) among those without an OP ($p = 0.02$). Logistic regression analysis also showed that bladder volumes below 150 ml decreased the possibility of achieving an OP. However, the percentage of patients with an OP showed a plateau effect at bladder volumes above 150 ml. *Conclusions.* Bladder volume is a significant factor affecting OP rates. However, our results suggest that bladder volumes exceeding 150 ml may not help meet planning dose constraints.

The bladder is filled to various volumes during fractionated radiotherapy. Changing bladder volumes affects both bladder dose volumes and the position of adjacent organs (the prostate, seminal vesicles, small intestine and sigmoid colon) [1]. Furthermore, significant variations in bladder volume can affect planned three-dimensional conformal radiotherapy (3D-CRT) and intensity-modulated radiation therapy (IMRT) dose distributions. For all these reasons, bladder volumes must be kept consistent throughout planning and treatment to reduce positional uncertainties related to the prostate and the risk of increased toxicity to the surrounding normal tissue.

There is no current consensus regarding the optimal bladder volumes in definitive radiotherapy for localized prostate cancer. One possible advantage of maintaining a full bladder is that part of the bladder moves away from the target volume, thereby reducing bladder toxicity [2,3]. A full bladder also moves the small intestine and the sigmoid colon out of the irradiation field, reducing toxicity in these organs [1,4–7]. However, if we target larger bladder volumes on planning using computed tomography (CT) and during radiotherapy, such volumes tend to show marked variability [8–10]. On the other hand, excessively small bladder volumes make it difficult to meet planning dose constraints for the bladder and adjacent organs. For these reasons, the optimal bladder volume may be the minimum bladder volume that can satisfy dose constraints. Based on this reasoning, several institutions target a half-full bladder or a comfortably full bladder [8,9]. However, no previous

Correspondence: N. Nakamura, Department of Radiation Oncology, St. Luke's International Hospital, 9-1, Akashicho, Chuoh-ku, Tokyo 104-8560, Japan. Tel: +81 3 35415151. Fax: +81 3 35440649. E-mail: nnakamur-tky@umin.ac.jp

(Received 30 June 2011; accepted 4 November 2011)

ISSN 0284-186X print/ISSN 1651-226X online © 2011 Informa Healthcare
DOI: 10.3109/0284186X.2011.639388

reports have focused on the relationship between the bladder volume and optimal treatment planning.

We evaluated the relationship between the bladder volume on planning CT and the percentage satisfying the dose constraints as a reference what bladder volumes should be targeted.

Material and methods

Between June 2007 and February 2009, 243 patients underwent definitive radiotherapy with helical tomotherapy using the Hi-Art System (Tomotherapy Inc.) for intermediate- and high-risk localized prostate cancer (cT1-4N0M0) according to D'Amico's classification at Edogawa Hospital (Tokyo, Japan) (Table I).

The patients were irradiated in a supine position, with a knee support. They were instructed to refrain from urinating for 60–90 minutes before the planning computed tomography (CT) scan and before daily irradiation. They were also encouraged to drink an unspecified volume of water to ensure a clear but tolerable urge to urinate before the planning CT scan and before daily irradiation. They were instructed to take laxatives before the planning CT scan, although no specific instructions were issued regarding bowel movements before daily irradiation.

Table I. Patient characteristics.

	no.
cT stage (TNM 6th ed.)	
1–2a	101(42%)
2b	32 (13%)
2c	40 (16%)
3a	61 (25%)
3b	8 (33%)
4	1 (0.4%)
Gleason score	
2–6	41 (17%)
7	102 (42%)
8–10	100 (41%)
Pretreatment PSA	
0–10	104 (43%)
10–20	67 (28%)
>20	72 (30%)
D'Amico's risk group	
Intermediate	71 (29%)
High	172 (71%)
Neoadjuvant hormone therapy	
No	81 (33%)
Yes	162 (67%)
Mean age (range)	70 (42–85)
Mean prostate volume (range)	21 ml (6–178)
Mean PTV (range)	112 ml (61–273)
Mean bladder volume (range)	235 ml (45–653)

cT stage, clinical tumor stage; PSA, prostate-specific antigen; PTV, planning target volume.

The clinical target volume (CTV) was defined as the prostate that was delineated by the fusion images of CT and magnetic resonance imaging (MRI) with a 5-mm margin and 2 cm of the proximal seminal vesicle. Exceptionally, the whole seminal vesicle was included in the CTV for cases of clinical T3b stage disease. The planning target volume (PTV) was defined as the CTV with a 5-mm margin. The prescribed dose defined as 95% of the PTV receiving ≧ 100% of the prescription dose (D95) was 76 Gy in 38 fractions. The treatment plans were optimized to satisfy the dose constraints defined by in-house protocols for the PTV and organs at risk (OAR) (Table II). No specific protocols were used for the order of prioritization among the constraints. Cases in which all dose constraints were satisfied were defined as an optimal plan (OP).

We assessed the relationship between the bladder volumes on planning CT and the percentage of patients achieving an OP. Univariate logistic regression analysis was used to examine the predictive value of covariates including clinical T stage (T1–2a, T2b, T2c, T3a, T3b, and T4), Gleason score (2–6, 7, 8–10), pretreatment PSA (0–10, 10–20, and > 20), D'Amico's risk group (intermediate or high), neoadjuvant hormone therapy (yes or no), age, PTV, and bladder volume. Those showing significant associations in univariate logistic regression analysis were further tested by multivariate logistic regression analysis.

We used GraphPad Prism version 5 (GraphPad Software Inc.) and SPSS version 17 (IBM) for statistical analysis. Differences were deemed significant when two-tailed p-values were less than 0.05.

Results

Of the subjects, 203 patients (84%) met the definitions for an OP. Among these patients, the mean of

Table II. Dose constraints.

Target/Organ		Dose constraint
PTV	D95	100% (76 Gy)
	Maximum	< 110% (83.6 Gy)
	Mean	< 105% (79.8 Gy)
Rectum wall*	V40	< 65%
	V60	< 35%
	V70	< 25%
	V78	< 10%
Bladder wall	V40	< 60%
	V70	< 35%
Sigmoid colon	V65	< 0.5 ml
Small bowel	V60	< 0.5 ml

*Rectum wall within 5 mm above and below the PTV, Vx < y% (or ml) means that no more than y% (or ml) of the volume of the organ receive a dose > x Gy.
PTV, planning target volume.

the mean PTV dose and the maximum dose were 77.4 Gy (range 76.7–79.2 Gy) and 80.7 Gy (range 78.2–83.3 Gy), respectively.

The mean bladder volume (±1 standard deviation; SD) was 266 ml (±130 ml) among those with an OP and 214 ml (±130 ml) among those without an OP ($p = 0.02$, by unpaired t-test).

Logistic regression analysis also showed that bladder volumes below 150 ml decreased the possibility of achieving an OP (Table III). Figure 1 shows the percentage of patients with an OP according to bladder volumes, indicating that the percentage of patients with an OP showed a plateau effect at bladder volumes above 150 ml. On univariate analysis, higher clinical T stage, younger age, treatment with neoadjuvant hormone therapy, and larger bladder volume were predictors for achieving an OP (Table IV). On multivariate analysis, larger bladder volumes ($p = 0.04$), younger age ($p = 0.01$), and higher clinical T stage ($p = 0.03$) were independent predictors for achieving an OP.

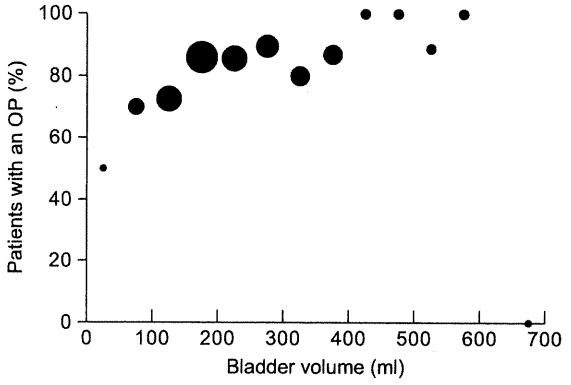

Figure 1. The percentage of patients with an OP according to bladder volume. Patients were divided into subgroups according to their bladder volume by 50 ml. The percentage of patients with an OP was defined by dividing the number of patients with an OP by the number of patients in each subgroup. The size of each dot represents the number in each subgroup.
n, number of patients; OP, optimal plan.

Discussion

We found that bladder volumes among patients with an OP were significantly larger than among patients without an OP. This indicates that bladder volume is a significant factor affecting whether OP is achieved. However, we also found that bladder volumes larger than 150 ml did not contribute to OP rates. We could meet the dose constraints on the bladder even with considerably small bladder volumes. However, small bladders moved the small intestine and the sigmoid colon inside the irradiation field, which made it impossible to meet the dose constraint on those organs. This may explain why we found the plateau effect at bladder volumes above 150 ml.

Table III. Logistic regression analysis between bladder volume and the percentage of patients with an optimal plan.

Bladder volume	Number of patients	Patients with an OP	p	Odds ratio (95% CI)
<100 ml	21	15 (71%)	0.069	0.34 (0.11–1.09)
100–149 ml	34	24 (71%)	0.028	0.33 (0.12–0.89)
150–199 ml	43	37 (86%)	0.761	0.85 (0.29–2.50)
200–249 ml	35	30 (86%)	0.739	0.82 (0.26–2.61)
250–299 ml	27	24 (89%)	0.896	1.10 (0.28–4.31)
>300 ml	83	73 (88%)		1

OP, optimal plan.

Our logistic regression analysis did not show a statistically significant difference in the percentage of patients with an OP in the subgroup with the smallest bladder volume. We think the relatively small number of subjects in the subgroup caused the false negative.

Our results suggested that younger age and higher clinical T stage were also independent predictors for achieving an OP. It is difficult to interpret why age affects OP achievement. There may be some anatomic features among younger patients that make it easier to achieve an OP. It is also difficult to interpret why clinical T stage affects OP achievements although we used the same definition of CTV for all clinical T stages except for the few cases of clinical T3b.

The existence of a clear dose effect for genitourinary (GU) toxicity is well-known in cases in which the entire bladder is irradiated [11]. In the case of prostate irradiation, the cranial portion of the bladder is generally spared, whereas the bladder neck and urethra are irradiated at levels close to the prescribed dose. Most of the published results fails to support a correlation between bladder dose volume histograms (DVH) and GU toxicity [12,13], whereas several studies indicate that the absolute volume of the bladder receiving >78 Gy to 80 Gy is most predictive of late GU toxicity [14,15]. Regarding GU toxicity, a half-full bladder and an empty bladder appear to be acceptable bladder volumes [16]. However, an excessively small bladder volume may move the small intestine and sigmoid colon within the high dose irradiated field [1,4–6]. Therefore, we also imposed dose constraints on the small intestine and sigmoid colon.

Table IV. Univariate logistic regression analysis of association with achieving an optimal plan.

	Patients with an OP (n, 203)	Patients without an OP (n, 40)	p
cT stage (TNM 6th ed.)			0.03
1–2a	77 (38%)	24 (60%)	
2b	26 (13%)	6 (15%)	
2c	35 (17%)	5 (13%)	
3a	57 (28%)	4 (10%)	
3b	7 (3%)	1 (3%)	
4	1 (0.5%)	0 (0%)	
Gleason score			NS
2–6	39 (19%)	2 (5%)	
7	83 (41%)	19 (48%)	
8–10	81 (40%)	19 (48%)	
Pretreatment PSA			NS
0–10	85 (42%)	19 (48%)	
10–20	58 (28%)	9 (23%)	
>20	60 (30%)	12 (30%)	
D'Amico's risk group			NS
Intermediate	60 (30%)	11 (28%)	
High	143 (70%)	29 (73%)	
Neoadjuvant hormone therapy			0.10
No	63 (31%)	18 (45%)	
Yes	140 (69%)	22 (55%)	
Mean age (range)	70 (42–85)	73 (59–83)	0.01
Mean prostate volume (range)	21 ml (6–178)	22 ml (12–103)	NS
Mean PTV (range)	109 ml (61–225)	115 ml (77–273)	NS
Mean bladder volume (range)	266 ml (45–594)	214 ml (48–653)	0.04

cT stage, clinical tumor stage; OP, optimal plan; PSA, prostate-specific antigen; PTV, planning target volume.

Several previous studies have reported that the greatest variation in bladder volume is found in patients with large initial bladder volumes [8,9,17]. Significant variations in bladder volume can confound planned dose distributions. A half-full bladder of 150 ml or slightly larger may represent a reasonable target, offering the potential to improve bladder volume consistency without compromising the dose constraints for the adjacent organs.

A limitation of this investigation is the lack of the clinical correlation. We need to investigate the correlation between bladder volumes on planning CT and clinical outcomes in a future study. In most cases, we use a shrinking PTV if we can not satisfy the dose constraints for OARs. Our concern is that the compromise might cause inferior local control and survival rates. However, long-term follow-up is necessary to clarify the clinical impact. We consider achieving an optimal plan a surrogate marker for clinical outcomes; therefore, we report the correlation between bladder volumes and achieving an optimal plan as the first step.

While optimal bladder volumes vary from institution to institution according to the protocol used, we believe that each institution must seek to recognize what bladder volumes are optimal in definitive radiotherapy for localized prostate cancer.

In conclusions, bladder volume is a significant factor affecting the achieving of an optimal plan. However, our results suggest that bladder volumes exceeding 150 ml may not help meet planning dose constraints.

Acknowledgements

A portion of this report was presented at the 52nd Annual Meeting of the American Society of Therapeutic Radiology and Oncology at San Diego, October 31–November 4, 2010. The authors report no conflicts of interest. The authors alone are responsible for the content and writing of the paper.

Declaration of interest: The authors report no conflicts of interest. The authors alone are responsible for the content and writing of the paper.

References

[1] De Meerleer GO, Villeirs GM, Vakaet L, Delrue LJ, De Neve WJ. The incidence of inclusion of the sigmoid colon and small bowel in the planning target volume in radiotherapy for prostate cancer. Strahlenther Onkol 2004;180:573–81.

[2] Emami B, Lyman J, Brown A, Coia L, Goitein M, Munzenrider JE, et al. Tolerance of normal tissue to therapeutic irradiation. Int J Radiat Oncol Biol Phys 1991;21:109–22.

[3] Marks LB, Carroll PR, Dugan TC, Anscher MS. The response of the urinary bladder, urethra, and ureter to radiation and chemotherapy. Int J Radiat Oncol Biol Phys 1995;31: 1257–80.

[4] Brierley JD, Cummings BJ, Wong CS, McLean M, Cashell A, Manter S. The variation of small bowel volume within the pelvis before and during adjuvant radiation for rectal cancer. Radiother Oncol 1994;31:110–6.

[5] Kim TH, Chie EK, Kim DY, Park SY, Cho KH, Jung KH, et al. Comparison of the belly board device method and the distended bladder method for reducing irradiated small bowel volumes in preoperative radiotherapy of rectal cancer patients. Int J Radiat Oncol Biol Phys 2005;62: 769–75.

[6] Muren LP, Smaaland R, Dahl O. Organ motion, set-up variation and treatment margins in radical radiotherapy of urinary bladder cancer. Radiother Oncol 2003;69: 291–304.

[7] Waldenstrom AC, Alsadius D, Pettersson N, Johansson KA, Holmberg E, Steineck G, et al. Variation in position and volume of organs at risk in the small pelvis. Acta Oncol 2010;49:491–9.

[8] Stam MR, van Lin EN, van der Vight LP, Kaanders JH, Visser AG. Bladder filling variation during radiation treatment of prostate cancer: Can the use of a bladder ultrasound scanner and biofeedback optimize bladder filling? Int J Radiat Oncol Biol Phys 2006;65:371–7.

[9] O'Doherty UM, McNair HA, Norman AR, Miles E, Hooper S, Davies M, et al. Variability of bladder filling in patients receiving radical radiotherapy to the prostate. Radiother Oncol 2006;79:335–40.

[10] Nakamura N, Shikama N, Takahashi O, Ito M, Hashimoto M, Uematsu M, et al. Variability in bladder volumes of full bladders in definitive radiotherapy for cases of localized prostate cancer. Strahlenther Onkol 2010;186:637–42.

[11] Burman C, Kutcher GJ, Emami B, Goitein M. Fitting of normal tissue tolerance data to an analytic function. Int J Radiat Oncol Biol Phys 1991;21:123–35.

[12] Michalski JM, Winter K, Purdy JA, Wilder RB, Perez CA, Roach M, et al. Preliminary evaluation of low-grade toxicity with conformal radiation therapy for prostate cancer on rtog 9406 dose levels I and II. Int J Radiat Oncol Biol Phys 2003;56:192–8.

[13] Storey MR, Pollack A, Zagars G, Smith L, Antolak J, Rosen I. Complications from radiotherapy dose escalation in prostate cancer: Preliminary results of a randomized trial. Int J Radiat Oncol Biol Phys 2000;48:635–42.

[14] Harsolia A, Vargas C, Yan D, Brabbins D, Lockman D, Liang J, et al. Predictors for chronic urinary toxicity after the treatment of prostate cancer with adaptive three-dimensional conformal radiotherapy: Dose-volume analysis of a phase II dose-escalation study. Int J Radiat Oncol Biol Phys 2007; 69:1100–9.

[15] Cheung MR, Tucker SL, Dong L, de Crevoisier R, Lee AK, Frank S, et al. Investigation of bladder dose and volume factors influencing late urinary toxicity after external beam radiotherapy for prostate cancer. Int J Radiat Oncol Biol Phys 2007;67:1059–65.

[16] Fonteyne V, Villeirs G, Lumen N, De Meerleer G. Urinary toxicity after high dose intensity modulated radiotherapy as primary therapy for prostate cancer. Radiother Oncol 2009;92:42–7.

[17] Villeirs GM, De Meerleer GO, Verstraete KL, De Neve WJ. Magnetic resonance assessment of prostate localization variability in intensity-modulated radiotherapy for prostate cancer. Int J Radiat Oncol Biol Phys 2004;60:1611–21.

Radiotherapy and Oncology 100 (2011) 380–385

Contents lists available at SciVerse ScienceDirect

Radiotherapy and Oncology

journal homepage: www.thegreenjournal.com

Cone beam CT

4D-CBCT reconstruction using MV portal imaging during volumetric modulated arc therapy

Satoshi Kida, Naoya Saotome, Yoshitaka Masutani, Hideomi Yamashita, Kuni Ohtomo, Keiichi Nakagawa, Akira Sakumi, Akihiro Haga *

Department of Radiology, University of Tokyo Hospital, Japan

ARTICLE INFO

Article history:
Received 23 July 2011
Received in revised form 29 August 2011
Accepted 30 August 2011
Available online 29 September 2011

Keywords:
CBCT
4D-CT
Respiratory motion
Portal imaging
VMAT

ABSTRACT

Background: Recording target motion during treatment is important for verifying the irradiated region. Recently, cone-beam computed tomography (CBCT) reconstruction from portal images acquired during volumetric modulated arc therapy (VMAT), known as VMAT-CBCT, has been investigated. In this study, we developed a four-dimensional (4D) version of the VMAT-CBCT.

Materials and methods: The MV portal images were sequentially acquired from an electronic portal imaging device. The flex, background, monitor unit, field size, and multi-leaf collimator masking corrections were considered during image reconstruction. A 4D VMAT-CBCT requires a respiratory signal during image acquisition. An image-based phase recognition (IBPR) method was performed using normalised cross correlation to extract a respiratory signal from the series of portal images.

Results: Our original IBPR method enabled us to reconstruct 4D VMAT-CBCT with no external devices. We confirmed that 4D VMAT-CBCT was feasible for two patients and in good agreement with in-treatment 4D kV-CBCT.

Conclusion: The visibility of the anatomy in 4D VMAT-CBCT reconstruction for lung cancer patients has the potential of using 4D VMAT-CBCT as a tool for verifying relative positions of tumour for each respiratory phase.

Radiotherapy is complex and verification of treatment is crucial. Although portal images acquired during treatment with an electronic portal imaging device (EPID) have been used as a planar image guidance tool and for geometrical quality assurance, the recent development of EPID dosimetry has provided in vivo dosimetry verification [1–3]. A Linac-mounted kV-CBCT is a powerful tool for verifying anatomical positions [4,5]. Accompanying rotational treatment such as volumetric modulated arc therapy (VMAT), in-treatment kV-CBCT images that reflect the patient's treatment position can be acquired just after the treatment [6–8]. The four-dimensional (4D) version known as 'in-treatment 4D kV-CBCT' verifies the positions of targets, such as lung tumours, with respiratory motion [9]. Acquiring CBCT images during treatment requires an orthogonal imager and a Linac-mounted kV source, and the isocentre displacement of the kV beam from the treatment beam must be carefully considered. More importantly, in-treatment kV-CBCT could expose the patient to additional radiation.

Recently, CBCT reconstruction with portal images during VMAT or VMAT-CBCT has been investigated [10]. The advantages of VMAT-CBCT are (1) no additional radiation exposure and (2) reduced hardware requirements, making the VMAT-CBCT a promising tool for verification of irradiated areas and/or in vivo dosimetry.

The 4D version of CBCT still presents a problem in acquiring respiratory signals for portal images. Generally, there are two methods to synchronously measure a respiratory signal with image acquisition. One method uses an image-based phase recognition (IBPR) technique [11–13]. The other uses an external respiratory monitoring system (e.g. AZ-733V by Anzai Medical Cooperation and real-time position management by Varian Medical System) [14]. This study tested the IBPR technique. For kV-CBCT, a technique of tracking small regions through the time series of projection images based on a maximum normalised cross correlation (NCC) was developed [9]. With this technique, parameters such as the size of the area were adjusted for application to portal images.

This paper reports on the feasibility of using 4D VMAT-CBCT as a treatment verification tool in two lung cancer patients receiving VMAT. Validity was assessed by comparing the tumour positions between 4D VMAT-CBCT images and in-treatment 4D kV-CBCT images simultaneously acquired during VMAT delivery. The 4D VMAT-CBCT images were also evaluated with phantom testing.

* Corresponding author. Address: Department of Radiology, The University of Tokyo Hospital, 7-3-1 Hongo, Bunkyo-ku, Tokyo 113-8655, Japan.
E-mail address: haga-haga@umin.ac.jp (A. Haga).

0167-8140/$ - see front matter © 2011 Elsevier Ireland Ltd. All rights reserved.
doi:10.1016/j.radonc.2011.08.047

Methods and materials

Outlook of the 4D VMAT-CBCT reconstruction process

4D VMAT-CBCT reconstruction is performed as follows: VMAT for lung cancer was delivered with an Elekta Synergy accelerator operating at 6 MV. During beam delivery, portal images were sequentially collected by EPID with an interval of 0.46 s using Elekta iViewGT software. The portal image consists of 1024 × 1024 pixels with a size of 0.25 mm at the isocentre. At maximum, 256 projection images per reconstruction were obtained. In order to connect the portal images with the corresponding gantry angles, we employed a log file via the Elekta software protocol, iCom, which records the gantry angle information during treatment. This was followed by matching the multi-leaf collimator (MLC) shapes derived from the portal images with those from iCom.

The acquired portal images can include the shift due to the geometric non-idealities in the rotation of the gantry system. The geometric non-idealities were measured in advance for gantry angle intervals of 5 degrees by analysing 10 cm × 10 cm radiation fields; this correction (flex correction) was performed for each portal image. The response of EPID was also regularised by considering the background (BG), linearity of monitor unit (MU), and field size (output factor) effects. MLC masking correction was performed according to Poludniowski et al. [10]. The MLC masking correction extrapolates the data truncated by the MLC field shape to mitigate artifacts otherwise induced by the filter operation of the CBCT reconstruction algorithm. A value in the masked region can be adjusted arbitrarily if we are interested only in visual images, not quantitative densities, within the patient. We defined the masking factor as a ratio of the maximum pixel value. In this study, we applied masking factors of 0.56 and 0.76 for patients 1 and 2, respectively.

Reconstruction of 4D VMAT CT requires a respiratory phase in the system. In this study, portal-image based phase recognition (P-IBPR) was employed using NCC (see below). The periodic selection of portal images of only one specific respiratory phase enables image reconstruction for that phase. Projection images were classified into 4 phases and the reconstructions were performed with a filtered back-projection (FBP) algorithm. The sequential process was performed off-line.

Portal-image based phase recognition (P-IBPR)

The method proposed here employs NCC with limited areas between adjacent portal images. Several rectangular areas ($w \times h = 5 \times 100$ pixels) are placed sequentially within exposed fields on each frame of the portal images to account for tumour motion. While a rectangular area in the current frame is fixed, an area on the next frame is moved so that the NCC value of the two areas is maximised. Movement is limited to the cranio-caudal axis. The position of the rectangular area was set to the initial position with respect to each portal image (see Fig. 1). By performing

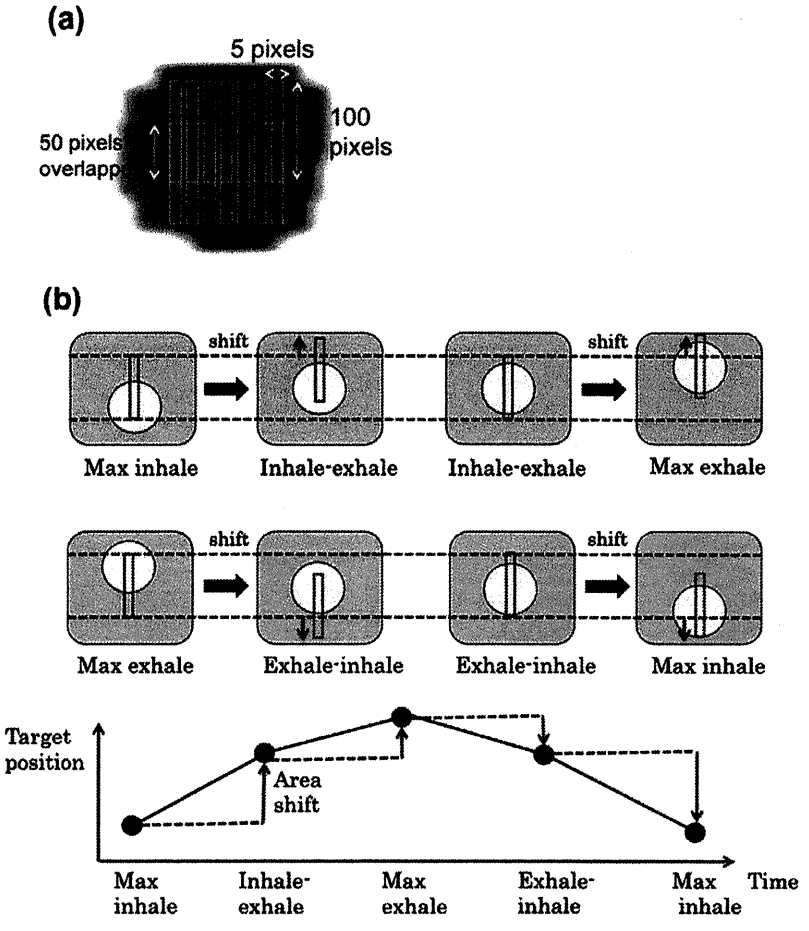

Fig. 1. (a) The distribution of several rectangular areas ($w \times h = 5 \times 100$ pixels) to cover tumour motion within exposed fields on each portal image. They are partially overlapped. (b) Schematic explanation of P-IBPR using NCC. The positions of the rectangular areas are shifted only along the cranio-caudal axis on the next portal image to find the maximum value of NCC with the calculation area on the previous portal image. The position of the rectangular area was set to the initial position with respect to each portal image. For the above example, the black rectangles indicate initial position and red rectangles indicate the position that gives the maximum NCC value with the corresponding black rectangles.

this procedure repeatedly for all portal images, a respiration signal can be obtained by displacement in the cranio-caudal direction. The signals were averaged among the calculation areas. Finally, low periodic components more than 5 s and high periodic components less than 1 s were removed in the frequency domain by using the band pass filter. The phase distributions were phase 0% (max inhale), phase 25% (inhale–exhale), phase 50% (max exhale), and phase 75% (exhale–inhale).

The efficiency of P-IBPR was determined by comparing the breathing pattern acquired by P-IBPR with those measured by visual tracking of the tumour on portal images. Here, the breathing cycle period was defined as the interval between adjacent max-expiration phases. In the visual tracking, a slight shaking can be recognised as a peak of expiration. Therefore, respirations with amplitudes less than 1 mm were neglected in the detection of max exhale.

Treatment planning for VMAT

One potential problem when inverse planning for lung cancer treatment is that the optimisation of beam fluences only takes into account a single three-dimensional volumetric data set. For this, the actual VMAT that continuously delivers the dose in all respiratory phases, may yield a dose distribution that differs from the plan. In order to compensate for this fact, the target volume can be extended to encompass the range of target motion by using 4D-CT scan, and field shapes can be defined as the target surroundings. Alternatively, the inverse plan that constrains MLC motion in VMAT forms field shapes that do not hide the target in lung cancer treatment. In this case, the beam intensity is mainly modulated by changing gantry speed and dose rate.

In this study, the planning target volume (PTV) for the lung tumour was created with a 5-mm margin of internal target volume generated from 20 4D-CT sets by using a 320-slice volumetric CT scanner (TOSHIBA, Japan). The patients received a D95 prescription of 50 Gy for PTV in 4 fractions. The single-arc VMAT with 6 MV was created by SmartArc in the Pinnacle v9.0 treatment planning system (Philips, USA). The constraint on MLC motion of 0.1 cm/degree was applied in the VMAT inverse plan so that MLC had little chance to hide the PTV. Such a constraint on MLC motion may significantly affect the quality of a treatment plan. Therefore, these plans were compared to those without constraints on MLC motion.

Treatment was performed by a single clockwise rotation (360 degrees). The arc used for reconstruction was from −180 to −19 degrees (patient 1) and from −180 to −40 degrees (patient 2). The angle range to allow portal imaging was limited by the Elekta iView software such that the maximum number of sequential acquisitions was 256. The difference between patients was due to the gantry speed determined by the VMAT plan.

Before applying the method to clinical cases, we conducted a 4D VMAT-CBCT reconstruction experiment by using the QUASAR respiratory motion phantom (Modus Medical Devices Inc.). The mechanical amplitude and cycle in the phantom were set at 10 mm and 3 s, respectively. The VMAT plan for patient 1 was delivered.

Result

VMAT plan with the MLC constraint

The dose-volume histograms (DVHs) for patients 1 and 2 are shown in Fig. 2a and b, respectively. The solid curves denote the DVHs with an MLC constraint of 0.1 cm/degree, while the dashed curves denote DVHs without MLC constraints. The dose homogeneity of the plan without MLC constraint was better than the plan with MLC constraint for both patients. Dose conformity was

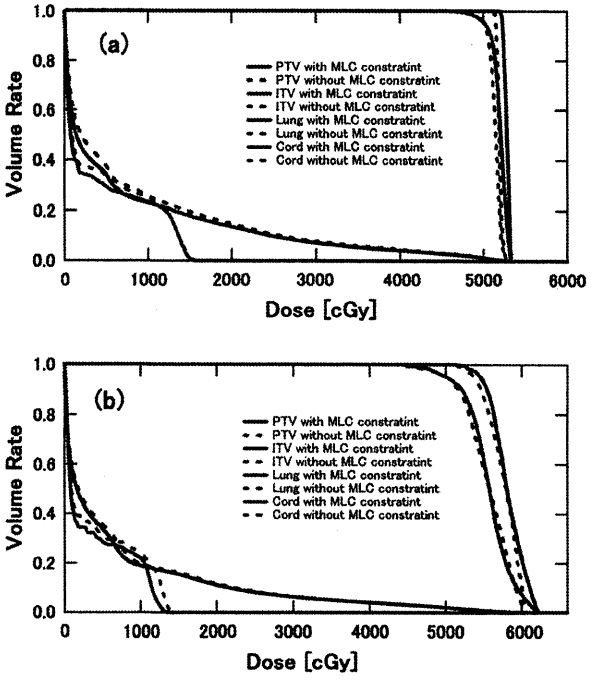

Fig. 2. DVH with and without MLC constraints for (a) patient 1 and (b) patient 2, All plans were prescribed as D95 of PTV equal to 50 Gy. The solid curves denote the DVHs with MLC constraint of 0.1 cm/degree, while the dashed curves denote those without MLC constraint.

comparable. On the other hand, the DVHs for organ at risk (OAR) with MLC constraint were slightly better than the DVHs without MLC constraint. This is presumably because in inverse planning, the constraint on homogeneity and conformity for PTV was stronger than the DVH constraint on OAR.

We found little difference between the plans with and without MLC constraints in the tested patients. The plans with MLC constraints were acceptable for clinical use and the MLC constraint was judged to manage the target motion without significant degradation of plan quality.

Acquisition of respiratory signal

The respiratory behaviours of two patients assessed by our P-IBPR method are shown in Fig. 3a and b. The original signal could have pseudo periodic components, such as those generated by gantry rotation. These components were removed by the band pass filter and, as seen in Fig. 3c and d, the motion due to patient respiration was clearly dissolved in all gantry angle directions. In Fig. 4, the breathing cycles were compared with those derived from the tumour motion in visual tracking. In Fig. 4a and b for patient 1, the breathing cycle was estimated by 3.7 ± 0.4 (1 SD) for both P-IBPR and visual tracking, while in Fig. 4c and d for patient 2, the breathing cycle was estimated by 2.7 ± 0.3 (1 SD) and 2.7 ± 0.4 (1 SD) for P-IBPR and visual tracking, respectively. The result in P-IBPR was concordant with the result of visual tracking. The difference of breathing cycle between P-IBPR and visual tracking was one sampling time (0.46 s) at most.

Reconstruction of 4D VMAT-CBCT in phantom

The reconstruction images of 4D VMAT-CBCT with an FBP algorithm corresponding to the points of maximum oscillation are shown in Fig. 5a and b. The standard calculation time for reconstruction with 270 × 270 × 80 voxels was about 10 s by GPU using

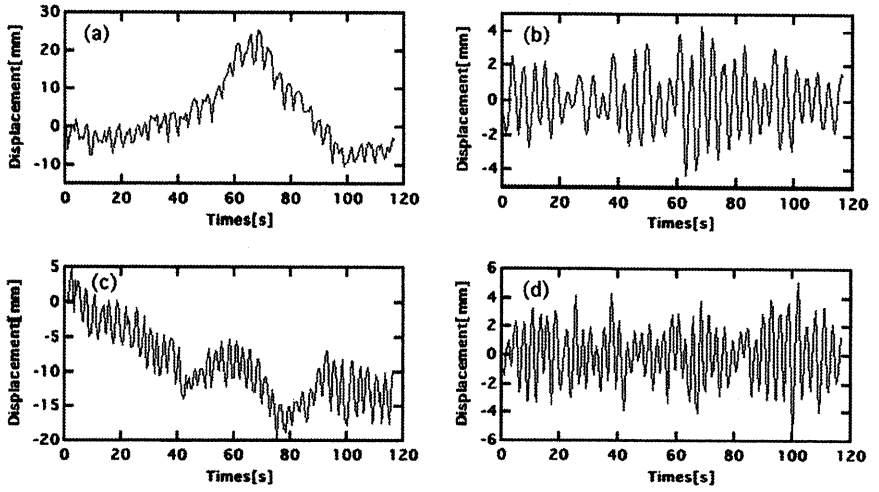

Fig. 3. Respiratory signal acquired by P-IBPR for patient 1 (a) before filtering and (b) after filtering and for patient 2 (c) before filtering and (d) after filtering.

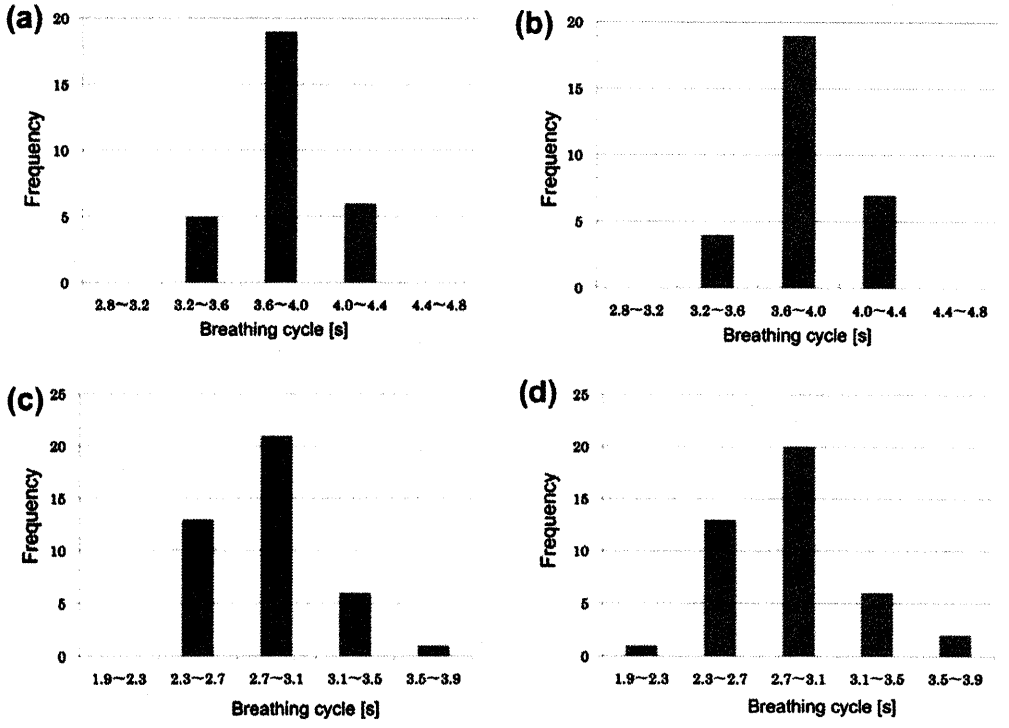

Fig. 4. Histograms of breathing cycle analysed by P-IBPR and visual tracking; (a) P-IBPR and (b) visual tracking for patient 1 and (c) P-IBPR and (d) visual tracking for patient 2.

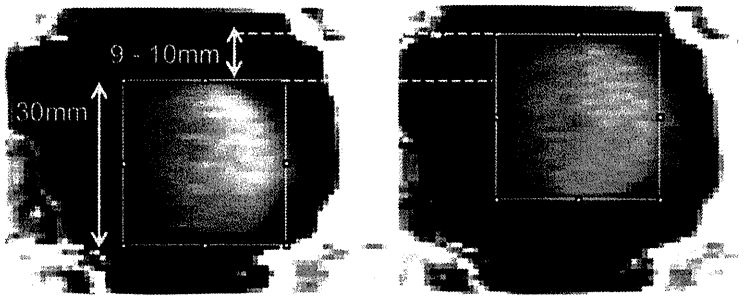

Fig. 5. Coronal images of 4D VMAT-CBCT of the QUASAR phantom in each peak. The diameter of the ball was 30 mm. The displacement was evaluated to be about 9–10 mm.

NAVIDIA Tesla C1060 4 GB. The amplitude was evaluated at about 9–10 mm from the 4D VMAT-CBCT images. This displacement is close to the mechanical set of 10 mm in the experiment. The inhomogeneous value inside the insert was observed.

Reconstruction of 4D VMAT-CBCT in 2 patients

With the respiratory signals acquired by P-IBPR, the portal images were classified into 4 phase bins. Then, VMAT-CBCT reconstruction was performed. For comparison, kV projection images were simultaneously acquired during VMAT, and 4D kV-CBCT was reconstructed. Fig. 6a and b illustrate the coronal and sagittal slices of VMAT-CBCT and kV-CBCT for 3D and the respiratory phases (max exhale, exhale inhale, max inhale, and inhale exhale) of patients 1 and 2.

The total number of portal images acquired during VMAT was 254 for both patients. Those images were almost equally classified into each phase bin. The gantry angle increment per projection for 4D reconstruction is dependent not only on the gantry speed but also on the respiratory cycle of the patient. These values for patients 1 and 2 were estimated as 5.4 ± 0.8 (1SD) and 3.9 ± 0.5 (1SD) degrees, respectively. Admittedly, there were large projection gaps that degraded image quality. In addition, this "effective" gantry angle increment included the error caused by the long acquisition interval of portal images, which was limited to 0.46 s per projection.

The centre of mass (COM) positions of the tumour during treatment were estimated from a contour of the tumour in respective max-exhale volume images in the Pinnacle treatment planning system and by shifting these contours in the other images. The shifts from the max exhale are denoted in Fig. 6. The results of 4D MV-CBCT were remarkably close to those of 4D kV-CBCT. The amplitudes of tumour motion during treatment for patients 1 and 2 were estimated to be about (1, 2, 5) and (2, 4, 5) mm, respectively. On the other hand, it was difficult to estimate tumour size due to diminished image quality and artifacts.

Discussion

It should be noted that an exact and unique cone-beam reconstruction from portal images acquired in a VMAT delivery is impossible in principle [10]. That is, the VMAT-CBCT including our method is based on the assumption that there are few structures outside the radiation field. The effect of passing through objects outside the reconstructed region is naively considered by masking correction. However, as seen in Figs. 5 and 6 4D VMAT-CBCT showed the tumour position to be similar when predicted mechanically by the phantom and by the 4D kV-CBCT. We emphasise that we are interested in the visualisation of tumour motion for verification of actual treatment. From this viewpoint, we are satisfied that the amplitude can be evaluated from the 4D VMAT-CBCT images. Our method is, therefore, feasible for verifying tumour motion through the course of treatment. On the other hand, it should be noted that inconsistencies, such as the lack of projection data provided the degradation of image quality, and may lead to incorrect recognition for the tumour size and shape.

We employed the IBPR method using NCC to derive respiratory signals from portal images. Our experiments demonstrated that NCC can work well for frame-by-frame changes in irradiation intensity. Respiratory signals were readily obtained because the MLC speed was constrained by treatment planning optimisation. This constraint yielded field shapes similar to those created in conformal treatment. The fact that the tumour was located in the middle of the lung may explain why the MLC did not need to move drastically. Thus, a target was detected within a field through

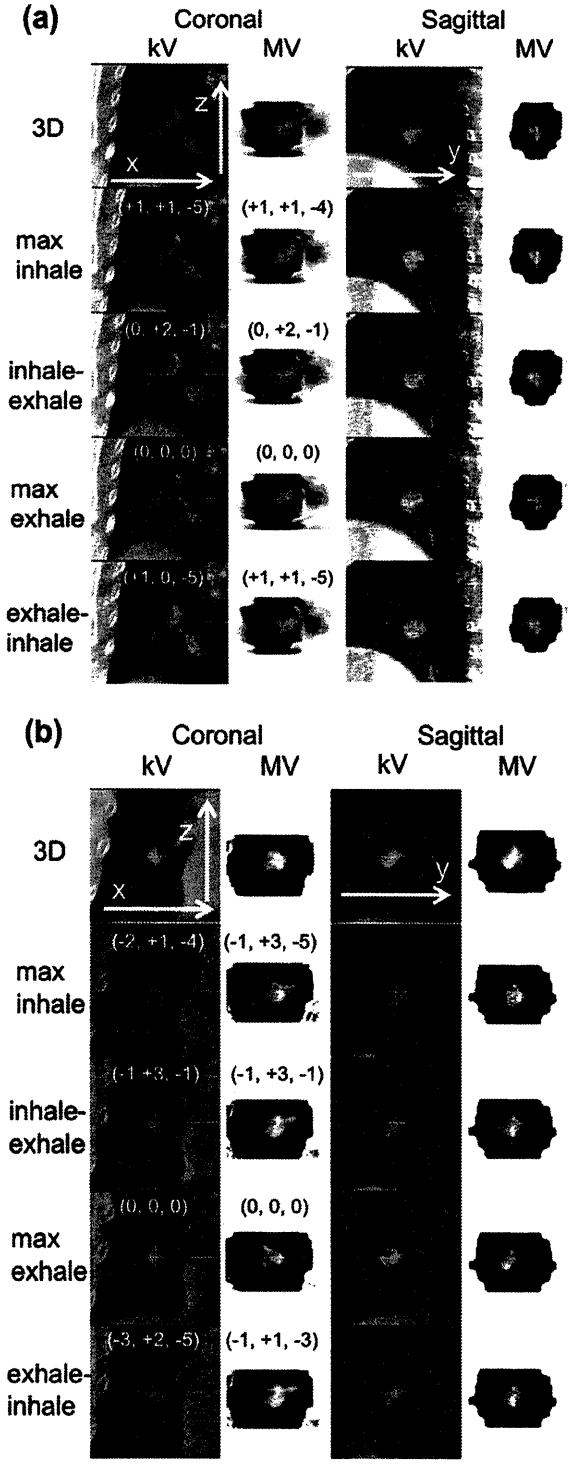

Fig. 6. Coronal and sagittal images at the isocentre plane of in-treatment kV 3D- and 4D-CBCT and 3D- and 4D-VMAT CT for (a) patient 1 and (b) patient 2. The coordinates inside the images represent the COM of tumour shift from max exhale with units in mm for each modality. The COMs were estimated from a contour delineated in respective max-exhale volume images on the Pinnacle treatment planning system and by shifting the contour in the other images.

almost all angles. On the other hand, the MLC constraint in the inverse plan may hinder clinical utility due to degradation of plan quality. In our clinical cases, this degradation was small and we judged that suppressing the MLC motion was beneficial for the

moving target. Of course, we cannot generalise our results, as this study was limited to 2 patients.

One of the advantages of IBPR is that no extra devices are required. It also provides direct tracking of tumour motion in contrast to methods that require external devices. In addition, correlations in the motion of inner structures and the body surface are not always measurable by external devices [15]. This is a critical problem for 4D-CT reconstruction.

In addition to our NCC method, several IBPR techniques such as the Amsterdam shroud method [11,12] and Kavanagh's method [13] have been proposed to acquire respiratory signals for kV projection images. The former projects 2D images onto the cranio-caudal axis to obtain a 1D signal for each image, while the latter utilises changes in the pixel value summation within each projection image. Both methods are based on pixel value projection and are easily affected by MLC motion, which yields drastic changes in pixel values within the projection images even if the MLC motion is as small as it was in our cases. Therefore, these methods would have difficulty with portal images.

Current issues or limitations of VMAT-CBCT reconstruction include the influence of intensity distribution and the shape yielded by MLC on the projection images. We performed a homogeneous correction of the total intensity within a field depending on the size and monitor unit. However, the change in field size yields an inhomogeneous intensity within the field, a matter that must be addressed in future studies. In addition, due to limitations of the Elekta iView software, the maximum number of portal imaging sequential acquisitions is only 256, so the acquisition of images may be insufficient for longer treatments. For stable P-IBPR, a sampling interval should be short enough to acquire a respiratory signal. Therefore, in this study, the shortest sampling rate of the Elekta iView software was employed, and the portal imaging was performed during less than half of a gantry rotation.

The inhomogeneous value inside the insert of the phantom as seen in Fig. 5 was also partly caused by this limitation. Optimised operation for the acquisition of portal images should be allowed in the system. Alternatively, a reconstruction algorithm can be developed as represented by digital tomosynthesis [16,17] and by compressed sensing [18] for a limited acquisition angle. The removal of such problems will enable quantitative derivation of 4D VMAT-CBCT.

In conclusion, a 4D VMAT-CBCT reconstruction technique was developed by using P-IBPR with the NCC method, which enabled us to obtain in-treatment volume images in 4 phases. The visibility of the anatomy in 4D VMAT-CBCT reconstruction for lung cancer patients makes this a promising tool for verifying relative tumour positions for each respiratory phase.

Acknowledgements

This work was partially supported by JSPS KAKENHI 22791176. S.K. and A.H. wish to thank Dr. Grant Jackson (Elekta K.K.) for his advice regarding the use of iCom to acquire log data during treatment. K.N. received research funding from Elekta K.K.

References

[1] van Elmpt W, McDermott L, Nijsten S, et al. A literature review of electronic portal imaging for radiotherapy dosimetry. Radiother Oncol 2008;88:289–309.
[2] Nijsten SM, Mijnheer BJ, Dekker AL, et al. Routine individualized patient dosimetry using electronic portal imaging devices. Radiother Oncol 2007;83:65–75.
[3] McDermott LN, Wendling M, Sonke JJ, et al. Replacing pretreatment verification with in vivo EPID dosimetry for prostate IMRT. Int J Radiat Oncol Biol Phys 2007;67:1568–77.
[4] Murphy MJ, Balter J, Balter S, et al. The management of imaging dose during image-guided radiotherapy: report of the AAPM Task Group 75. Med Phys 2007;34:4041–6063.
[5] Balter J, Benedict S, Bissonnette JP, et al. The role of in-room kV X-ray imaging for patient setup and target localization, AAPM Report No. 104. American Association of Physics in Medicine, 2009.
[6] Nakagawa K, Yamashita H, Shiraishi K, et al. Verification of in-treatment tumour position using kilovoltage cone-beam computed tomography: a preliminary study. Int J Radiat Oncol Biol Phys 2007;69:970–3.
[7] Nakagawa K, Haga A, Shiraishi K, et al. First clinical cone-beam CT imaging during volumetric modulated arc therapy. Radiother Oncol 2009;90:422–3.
[8] Ling C, Zhang P, Etmektzoglou T, et al. Acquisition of MV-scatter-free kilovoltage CBCT images during RapidArc™ or VMAT. Radiother Oncol 2011;100:145–9.
[9] Nakagawa K, Kida S, Haga A, et al. Cone beam computed tomography data acquisition during VMAT delivery with subsequent respiratory phase sorting based on projection image cross-correlation. J Radiat Res (Tokyo) 2011;52:112–3.
[10] Poludniowski G, Thomas MDR, Evans PM, et al. CT reconstruction from portal images acquired during volumetric-modulated arc therapy. Phys Med Biol 2011;55:5635–51.
[11] Sonke JJ, Zijp L, Remeijer P, van Herk M. Respiratory correlated cone beam CT. Med Phys 2005;32:1176–86.
[12] Zijp L, Sonke J, van Herk M. Extraction of the respiratory signal from sequential thorax cone-beam X-ray images. Jeong Publishing (Seoul) 2004:507–9.
[13] Kavanagh A, Evans PM, Hansen VN, et al. Obtaining breathing patterns from any sequential thoracic X-ray image set. Phys Med Biol 2009;54:4879–88.
[14] Otani Y, Fukuda I, Tsukamoto N, et al. A comparison of the respiratory signals acquired by different respiratory monitoring systems used in respiratory gated radiotherapy. Med Phys 2010;37:6178–86.
[15] Korreman SS, Juhler-Nottrup T, Boyer AL. Respiratory gated beam delivery cannot facilitate margin reduction, unless combined with respiratory correlated image guidance. Radiother Oncol 2008;86:61–8.
[16] Maurer J, Godfrey D, Wang Z, et al. On-board four-dimensional digital tomosynthesis: first experimental results. Med Phys 2008;35:3574–83.
[17] Maurer J, Pan T, Yin FF. Slow gantry rotation acquisition technique for on-board four-dimensional digital tomosynthesis. Med Phys 2010;37:921–33.
[18] Choi K, Wang J, Zhu L, et al. Compressed sensing based cone-beam computed tomography reconstruction with a first-order method. Med Phys 2010;37:5113–25.

ELSEVIER

Int. J. Radiation Oncology Biol. Phys., Vol. ■, No. ■, pp. 1–4, 2011

0360-3016/$ - see front matter

doi:10.1016/j.ijrobp.2010.11.046

CLINICAL INVESTIGATION

OUTCOMES OF DIFFUSION TENSOR TRACTOGRAPHY–INTEGRATED STEREOTACTIC RADIOSURGERY

TOMOYUKI KOGA, M.D.,* KEISUKE MARUYAMA, M.D., PH.D.,* KYOUSUKE KAMADA, M.D., PH.D.,* TAKAHIRO OTA, M.D., PH.D.,* MASAHIRO SHIN, M.D., PH.D.,* DAISUKE ITOH, M.D., PH.D.,† NAOTO KUNII, M.D.,* KENJI INO, R.T.,† ATSURO TERAHARA, M.D., PH.D.,† SHIGEKI AOKI, M.D., PH.D.,† YOSHITAKA MASUTANI, PH.D.,† AND NOBUHITO SAITO, M.D., PH.D.*

Departments of *Neurosurgery and †Radiology, University of Tokyo Hospital, Tokyo, Japan

Purpose: To analyze the effect of use of tractography of the critical brain white matter fibers created from diffusion tensor magnetic resonance imaging on reduction of morbidity associated with radiosurgery.
Methods and Materials: Tractography of the pyramidal tract has been integrated since February 2004 if lesions are adjacent to it, the optic radiation since May 2006, and the arcuate fasciculus since October 2007. By visually confirming the precise location of these fibers, the dose to these fiber tracts was optimized. One hundred forty-four consecutive patients with cerebral arteriovenous malformations who underwent radiosurgery with this technique between February 2004 and December 2009 were analyzed.
Results: Tractography was prospectively integrated in 71 of 155 treatments for 144 patients. The pyramidal tract was visualized in 45, the optic radiation in 22, and the arcuate fasciculus in 13 (two tracts in 9). During the follow-up period of 3 to 72 months (median, 23 months) after the procedure, 1 patient showed permanent worsening of preexisting dysesthesia, and another patient exhibited mild transient hemiparesis 12 months later but fully recovered after oral administration of corticosteroid agents. Two patients had transient speech disturbance before starting integration of the arcuate fasciculus tractography, but no patient thereafter.
Conclusion: Integrating tractography helped prevent morbidity of radiosurgery in patients with brain arteriovenous malformations. © **2011 Elsevier Inc.**

Arteriovenous malformation, Diffusion tensor tractography, Gamma knife, Morbidity, Stereotactic radiosurgery.

INTRODUCTION

Stereotactic radiosurgery is one of the principal treatment modalities for various kinds of vascular, neoplastic, or functional disorders of the brain (1–4). Although its efficacy is well known, radiation-induced neuropathy occurs in 5–20% of patients (2, 5–8). To minimize such unignorable risk, we have integrated tractography of the brain white matter based on diffusion tensor magnetic resonance imaging before the procedure into treatment planning of radiosurgery using Gamma Knife (9–11). Diffusion tensor tractography, one of the major recent advancements in magnetic resonance imaging, enables clear visualization of various fibers inside the white matter of the brain, which is not visible with use of conventional imaging modalities (12). Clinical applications of diffusion tensor tractography are mainly reported as diagnostic tools, and reports on its therapeutic application are quite limited (10, 13). In this study, we analyzed the effect of integrating diffusion tensor tractography into treatment planning of stereotactic radiosurgery on the reduction of morbidity in a prospective case series with arteriovenous malformations of the brain.

METHODS AND MATERIALS

Our selection criterion for stereotactic radiosurgery was, in principle, small malformations (<3 cm) in critical, or eloquent, areas of the brain (including sensorimotor, language, or visual cortex; the hypothalamus or thalamus; the internal capsule; the brain stem; the cerebellar peduncles; and the deep cerebellar nuclei) that, if injured, result in disabling neurologic deficits (2, 14). We started integrating diffusion tensor tractography of the pyramidal tract in February 2004 because we considered the pyramidal tract to be the most crucial fiber in preventing morbidity of radiosurgery out of complexity of white matter fibers inside the brain. From May 2006, we added the integration of diffusion tensor tractography of the optic radiation, and diffusion tensor tractography of the arcuate fasciculus tractography from October 2007. One hundred forty-four patients with arteriovenous malformations who have consecutively undergone stereotactic radiosurgery using Gamma Knife with this protocol between February 2004 and December

Reprint requests to: Tomoyuki Koga, M.D., Department of Neurosurgery, University of Tokyo Hospital, 7-3-1 Hongo, Bunkyo-ku, Tokyo 113-8655, Japan. Tel: (+81) 3-5800-8853; Fax: (+81) 3-5800-8655; E-mail: kouga-tky@umin.ac.jp

Conflicts of interest: none.
Received Sept 22, 2010, and in revised form Sept 22, 2010. Accepted for publication Nov 4, 2010.

Table 1. Baseline characteristics of 144 patients treated

Age (y)	35 (5–77)
Female sex	65 (45)
Details of arteriovenous malformations	
Diameter (cm)	2.7 (0.7–7.9)
Small size	89 (62)
Eloquent brain location	66 (46)
Deep venous drainage	74 (51)
Spetzler-Martin grade	II (I–VI)
Details of radiosurgery	
Target volume (cm^3)	6.9 (0.3–24)
Maximal dose (Gy)	40 (32–50)
Dose to margins (Gy)	20 (15–25)
Follow-up period (mo)	23 (3–72)

Data are number (percentage) or median (range).

2009 were enrolled in this study. All patients were considered as candidates for integrating tractography, but the integration was not carried out if a target lesion was considered to be located more than 1 cm apart from these fiber tracts and risk of injuring them was considered to be sufficiently low. Malformations were located in eloquent brain areas in 66 patients (46%). Detailed treatment parameters are shown in Table 1.

Diffusion tensor magnetic resonance imaging was obtained on the day before treatment. Tractography was created from diffusion tensor imaging by using freely shared programs, according to anatomic landmarks as shown in previous studies (9–12).

On the day of treatment, patients were affixed to the stereotactic coordinate frame and underwent stereotactic magnetic resonance imaging and stereotactic cerebral angiography. Stereotactic magnetic resonance imaging and tractography were registered by using the method reported previously (9–11, 15). After the introduction of Gamma Knife 4C in October 2006, the registration process was automated (16). Tractography-integrated images were imported to treatment planning images on the day of radiosurgery. Conformal treatment planning was made by experienced neurosurgeons and radiation oncologists with use of the treatment planning software GammaPlan (Elekta Instruments AB, Stockholm, Sweden). Generally 20 Gy was given to the margin of lesions by using 40–50% isodose lines. Any portion of the anterior visual pathway and half of the brainstem were designed to receive no more than 10 Gy.

The precise location of the pyramidal tract (Fig. 1), the optic radiation (Fig. 2), or the arcuate fasciculus was confirmed on treatment planning images, and it was attempted that the maximum dose received by each fiber was less than 20 Gy, 8 Gy, or 8 Gy (20 Gy in the frontal fibers), respectively, on the basis of previous analyses (9–11), though this was not possible in some cases.

Serial formal neurologic and radiologic examination was performed every 6 months after the procedure.

RESULTS

Diffusion tensor–based tractography was prospectively integrated in 71 (46%) of 155 treatment sessions. Integrated fiber tracts were the pyramidal tract in 45, the optic radiation in 22, and the arcuate fasciculus in 13 sessions, including 9 in which two tracts were integrated (the pyramidal tract and the optic radiation in 2, the pyramidal tract and the arcuate fasciculus in 3, the optic radiation and the arcuate fasciculus in 4). The optic radiation could not be depicted in 1 patient, and only arcuate fasciculus was drawn. Of 71 treatments with integration of tractography, the distance between the lesion and critical white matter fibers was less than 5 mm in 43 (60%); thus, tighter treatment planning was mandatory. Consequently, 39 sessions (55%) necessitated any modification in treatment planning by reducing the radiation dose to the visualized tracts. Until December 2007, 38% of treatments (37 of 98 sessions) were performed with integration of tractography, whereas tractography was integrated for 60% (34 of 57) thereafter. This difference in frequency was statistically significant according to χ^2 test ($p = 0.008$).

Two patients died of unknown cause after the procedure. The other 142 patients were followed for 3–72 months (median, 23 months) after radiosurgery. During this period, transient speech disturbance was observed in 2 patients. They were treated before 2007, when we started integrating arcuate fasciculus tractography. One patient with right thalamic arteriovenous malformation showed gradual worsening of pre-existing dysesthesia of left upper and lower extremities after treatment, and this symptom lasted until the last

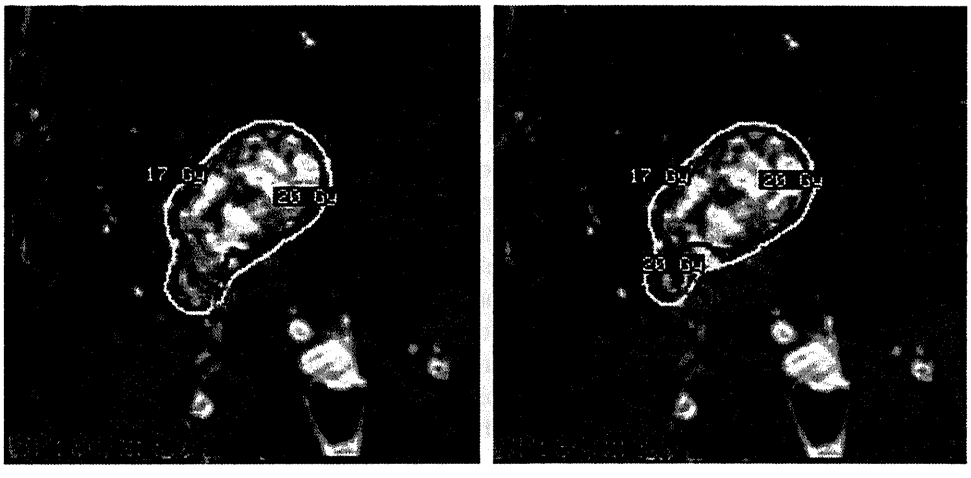

Fig. 1. Radiosurgical dosimetry of 23-year-old woman with ruptured arteriovenous malformation in the right basal ganglia. Dose delivered to the corticospinal tract before referring to tractography (a) was intentionally reduced after its integration (b).